

# Fabrication of Fe-doped ZnO/Nanocellulose Nanocomposite as an Efficient Photocatalyst for Degradation of Methylene Blue Under Visible Light

Mohammad Saeed Vasheghani Farahani

Babol Noshirvani University of Technology

Maryam Nikzad (✉ [m.nikzad@nit.ac.ir](mailto:m.nikzad@nit.ac.ir))

Babol Noshirvani University of Technology <https://orcid.org/0000-0001-5143-3111>

Mohsen Ghorbani

Babol Noshirvani University of technology

---

## Research Article

**Keywords:** Nanocellulose, Broom corn stalk, Photocatalytic degradation, Methylene blue, Fe-doped ZnO.

**Posted Date:** January 7th, 2022

**DOI:** <https://doi.org/10.21203/rs.3.rs-1049927/v1>

**License:**  This work is licensed under a Creative Commons Attribution 4.0 International License.

[Read Full License](#)

---

# Abstract

In this work, a photocatalytic nanocomposite, Fe-doped ZnO/nanocellulose, was synthesized using an *in-situ* method and examined for methylene blue (MB) degradation. For this purpose, pure ZnO (PZ) was synthesized by the chemical precipitation method and then subjected to Fe<sup>3+</sup> doping with different concentrations of Fe<sup>3+</sup> (1, 3, and 5 mol%). The PZ and Fe-doped ZnO (FZ) samples were characterized using several standard analyses. UV-vis DRS analysis was also used to investigate the effect of Fe<sup>3+</sup> doping on the bandgap of PZ. The doping of Fe<sup>3+</sup> enhanced the photocatalytic activity of ZnO under visible light. The degradation efficiency of FZ samples (> 50%) was enhanced compared to the pristine ZnO (36.91%) during the same period. The catalyst with the highest degradation efficiency (94.21%) was then conjugated with broom corn stalk-derived nanocellulose (NC) at varying NC/ Zn<sup>2+</sup> molar ratios (0.1, 0.2, 0.3, and 0.4) and characterized by various analyses. The NC enhanced the hydroxyl group at the surface of the nanocomposite, consequently improved the photocatalytic performance of the synthesized samples. The ability of the optimized photocatalyst for MB degradation was assessed. The effect of operating parameters such as pH, catalyst dosage, and initial MB concentration was investigated and degradation efficiency of 98.84% was achieved at the optimum condition. Besides, photocatalyst regeneration study indicated the great photocatalytic performance of this nanocomposite with no loss in its degradation efficiency. The facile synthesis and fast degradation rate of this nanocomposite make it a promising candidate for real-world wastewater treatment.

# Introduction

Over the past few decades, the discharge of industrial effluents into water bodies has raised environmental concerns (Nagaraju et al. 2020). Dyes are one of the most prominent pollutants that display an increasing ecological threat. Different industries such as textile, leather tanning, plastics, cosmetics, and paint production are among the largest producers of colored effluents and create severe environmental pollution problems (Rajendran et al. 2020; Sirajudheen et al. 2020). Dyes are non-biodegradable compounds that reduce the aquatic plants' photosynthetic activity by preventing the penetration of light into the water and also contaminate the food chain because of their toxicity (Elfeky et al. 2020). Therefore, to keep the environment safe, it is necessary to remove dyes from contaminated effluents before being discharged to water resources.

Several conventional approaches consisting of flocculation-coagulation (Wang et al. 2020), membrane separation (Yang et al. 2020), adsorption (Saxena et al. 2020), biological treatment (Masoudnia et al. 2020), and ozonation (Muniasamy et al. 2020) have been used to remove dyes from aqueous solutions and industrial wastewaters. However, these methods need additional treatment to avoid secondary pollution (Emadian et al. 2020). Recently, advanced oxidation processes (AOPs) have been widely used for wastewater treatment (Abebe et al. 2020; Qi et al. 2017; Wang et al. 2019). Among AOPs, heterogeneous photocatalysis as an effective process has received great attention, thanks to its high efficiency, low cost, simple design, mild reaction condition, and environmental-friendliness (Chand et al.

2020; Flores et al. 2020). Semiconductor metal oxides such as ZnO, TiO<sub>2</sub>, Fe<sub>3</sub>O<sub>4</sub>, CuO, SnO<sub>2</sub>, and Bi<sub>2</sub>O<sub>3</sub> have been employed as photocatalyst in the wastewater treatment (Chand et al. 2020; Ciciliati et al. 2015; Evdokimova et al. 2020; Qi et al. 2017; Qi et al. 2020; Namini et al. 2021). Among them, ZnO has been extensively used in different applications because of its high catalytic activity, low cost, tunable morphology and non-toxicity (Wahid et al. 2019; Kim and Yong 2021). It has a wide bandgap of ~3.3 eV and a high exciton binding energy of 60 meV at room temperature with noble photochemical, optoelectronic, and piezoelectric properties (Ba-Abbad et al. 2013). However, ZnO suffers from some drawbacks such as the massive charge carrier recombination, large bandgap, high surface energy, photoinduced corrosion-dissolution at an extreme value of pH and poor visible light harvesting which limit the overall photocatalytic efficiency (Türkyılmaz et al. 2017). Due to the large bandgap energy, ZnO can be only activated under UV light irradiation, which constitutes approximately 5% of solar radiation (Yu and Yu 2008). To this end, many efforts have been dedicated to develop visible light active ZnO photocatalyst (Abdel-Wahab et al. 2016; Saffari et al. 2020; Sharma et al. 2020). Several strategies, such as tailoring the intrinsic defects, doping with transition metals and anionic non-metals, surface modification with organic compounds, noble metal deposition, hetero structuring with other semiconductors and modification with carbon nanostructures, have been successfully used to improve the photoactivity and stability of ZnO (Kumar and Rao 2015). Doping of ZnO with transition metals has been reported as an effective approach to improve ZnO photocatalytic properties under visible light (Qi et al. 2020; Shahbazkhany et al. 2020; Türkyılmaz et al. 2017). Fe-doped ZnO exhibited better photocatalytic activity than pure ZnO under visible light in many studies (Ba-Abbad et al. 2013; Ciciliati et al. 2015; Isai and Shrivastava 2019). This metal is one of the most common elements. Fe ion could act as a shallow electron trap in the lattice of photocatalyst that reduces the electron-hole recombination rate and enhances photocatalytic activity (Lavand and Malghe 2018). Hence, Fe was selected as the doping ion in this research.

Due to large surface area and high surface energy, ZnO nanoparticles (NPs) tend to aggregate which largely limits their photocatalytic activity (Jiang et al. 2020). To overcome this challenge, nanocomposites consisting of ZnO incorporated into natural polymers, such as cellulose (Abdalkarim et al. 2018), lignin (Zhang et al. 2020), chitosan (Kamal et al. 2015), and their derivatives (Jiang et al. 2020; Lizundia et al. 2018) have been developed. Cellulose is the most abundant, sustainable and renewable biopolymer that has been extensively employed in the synthesis of polymer nanocomposites (Ganguly and Lim 2020). It has attracted increasing attention, especially at nanoscale. Nanocellulose (NC), a promising natural material isolated from lignocellulosic materials, has excellent unique surface chemistry, physical properties, non-toxicity, biodegradability, and biocompatibility (Jiang et al. 2020). High concentration of hydroxyl groups on NC surface which can complex well with metal cations results in the homogenous dispersion of metal nanoparticles onto the NC matrix (An et al. 2020). Besides, surface modification of NC using sulfuric acid creates sulfate ester groups which replace hydroxyl groups and provide a highly charged surface that can act as an excellent template for the dispersion of Zn<sup>2+</sup> to prevent its aggregation (Moon et al. 2011). Recently, several studies reported the application of cellulose as a matrix for the fabrication of ZnO/cellulose composites (Elfeky et al. 2020; Fu et al. 2017; Lefatshe et

al. 2017). It has been shown that the hybridization of ZnO with NC improved its photocatalytic performance. Lefatshe et al. synthesized NC from oil palm empty fruit and used it as a host polymer for the fabrication of ZnO/cellulose nanocomposite. Results indicated that this nanocomposite exhibited a higher photocatalytic activity than pure ZnO nanostructure for the degradation of methylene blue (MB) (Lefatshe et al. 2017). Li et al. prepared ZnO/cellulose nanocomposites with adjustable photocatalytic properties. They used cellulose fibers with different aspect ratios and sizes for controlling the morphology of ZnO. They obtained ZnO with sheet, sphere, and flower-like morphologies via *in-situ* synthesis of cellulose fibers by a chemical deposition method. They found the flower-like ZnO supported on cellulose fiber displayed the best photocatalytic activity (Li et al. 2021). Guan et al. used bamboo crystalline nanocellulose (CNC) as a template for the fabrication of ZnO/CNC hybrid nanocomposite with modulated morphologies. They prepared this nanohybrid photocatalyst by a green one-step synthesis approach and investigated the effect of pH values on the morphology, thermal stability, antibacterial efficiency and dye removal efficiency of the photocatalyst. Their results showed that the fabricated nanocomposite displayed higher thermal stability and removal efficiency than pure CNC (Guan et al. 2019). Although reports on the development of ZnO/nanocellulose composites as photocatalysts are numerous, additional doping of this nanocomposite to further improve its photocatalytic activity has been rarely reported. Li et al. prepared porous Al-doped ZnO-cellulose composite. They investigated the effect of cellulose fiber size on the composite structure and showed its important role in the photocatalytic properties of fabricated composite (Li et al. 2020). Xiao et al. prepared Fe/ZnO composite nanosheets by hydrothermal technique using nanofibrillated cellulose (NFC) as a template and then employed it for photocatalytic degradation of tetracycline in aqueous solution. Their results showed that the synthesized nanocomposites displayed superior physical adsorption and photodegradation efficiency than ZnO/NFC under UV light irradiation (Xiao, Zhang, Wei, Yu, et al. 2018). Nasiri et al. incorporated Au/ZnO nanoparticles into cellulose acetate (CA) matrix using phase inversion process. They studied the effect of Au/ZnO nanoparticles on the morphology of cellulose-based nanocomposite. They reported that the porosity of CA/Au/ZnO nanocomposite was higher than the pure CA and the synthesized CA/Au/ZnO nanocomposite degraded Eosin Y, while no photocatalytic activity was obtained for the pure CA (Abad et al. 2020).

In this study, we aimed to investigate the photocatalytic activity of metal-biopolymer nanocomposite materials and designed a high-efficiency Fe-doped ZnO/nanocellulose (CFZ) composite as a new nanocomposite for MB degradation under visible light. To the best of authors' knowledge, there is no report on the fabrication of CFZ composite through *in situ* precipitation technique and the influence of NC concentration on the photocatalytic performance of the nanocomposite. In this work, broom corn stalk was used as feedstock for NC isolation. The NC and Fe-doped ZnO (FZ) were synthesized by acid hydrolysis and precipitation methods, respectively. The structural and morphological characteristics of the isolated NC, FZ and CFZ composite were determined by FTIR, FESEM, XRD, TEM, UV-vis DRS, and TG analyses. The photocatalytic activity of these materials for the degradation of MB, as the target pollutant, in the aqueous solution was examined. Moreover, the influence of different parameters such as pH, photocatalyst dosage, and initial dye concentration on the degradation of MB by CFZ composite was

investigated. In addition, the regeneration study was conducted to confirm the excellent performance of the fabricated nanocomposite.

## Materials And Methods

### Materials

Broomcorn (*Sorghum bicolor*) stalk (BS) was collected as waste from local broom making workshop in Amirkola (Babol, Iran) and used as feedstock for NC isolation. BSs were dehydrated at 60°C overnight. The dried BSs were cut into small pieces and subsequently ground using a grinder to obtain a fine BS. The ground BS was sieved through 20 mesh sieve and stored in a tight bag at room temperature for further experiments. The lignocellulosic composition of pristine BS was analyzed by a two-stage acid hydrolysis protocol developed by National Renewable Energy Laboratory (Sluiter et al. 2008), and the results are presented in Table 1. Zinc acetate dihydrate ( $\text{Zn}(\text{CH}_3\text{CO}_2)_2 \cdot 2\text{H}_2\text{O}$ ), iron trichloride hexahydrate ( $\text{FeCl}_3 \cdot 6\text{H}_2\text{O}$ ), sulfuric acid ( $\text{H}_2\text{SO}_4$ ), sodium hydroxide (NaOH), sodium chlorite ( $\text{NaClO}_2$ ), sodium carbonate ( $\text{Na}_2\text{CO}_3$ ), ethanol ( $\text{C}_2\text{H}_5\text{OH}$ ), methylene blue (MB), and other chemicals were purchased from Merck (Darmstadt, Germany). All the required chemicals were analytical grade and used as received without further purification.

Table 1  
Chemical composition of native broomcorn stalk

Component	wt%
Cellulose	44.2
Hemicellulose	23.5
Total lignin	22.7
Ash	4.1
Extractives	5.5

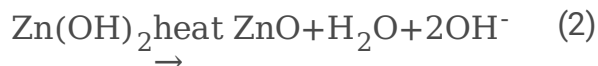
### Isolation of nanocellulose from BS

In this study, the NC was isolated from BS according to the methodology reported in our previous study (Langari et al. 2019). To remove non-cellulosic components (hemicellulose and lignin), the BS powder was subjected to alkali pretreatment and bleaching, as described in details in our previous study (Langari et al. 2019). The bleached BS (BBS) was subjected to acid hydrolysis. Initially, 5 g of BBS was hydrolyzed with 45 wt% sulfuric acid at 45°C for 75 min. Then, the hydrolysis reaction was quenched by adding 10 folds of cold distilled water to the reaction mixture. After precipitation of the suspension, the sediment was neutralized with 32 wt% sodium carbonate solution. Subsequently, the precipitate was centrifuged for 20 min at 9000 rpm several times to eliminate the remaining acid. Finally, the obtained sample was

dispersed in water and sonicated with ultrasonic homogenizer at an output power of 400 W, and a frequency of 20 kHz. The colloidal suspension was filtered and freeze-dried to obtain NC powder. Fig. 1. shows the schematic presentation of the NC isolation from BS by ultrasonic-assisted acid hydrolysis process.

## Preparation of ZnO and Fe/ZnO NPs

Pure ZnO and Fe/ZnO nanoparticles were prepared by the chemical precipitation method. Initially, the required stoichiometric amounts of  $\text{Zn}(\text{CH}_3\text{CO}_2)_2 \cdot 2\text{H}_2\text{O}$  and  $\text{FeCl}_3 \cdot 6\text{H}_2\text{O}$  were dissolved in 50 ml of deionized water depending on the percentage of Fe doping. The mixture was heated at 65°C under constant magnetic stirring to obtain a homogeneous solution. Thereafter, about 50 ml of 1M NaOH solution was added dropwise to the solution to attain pH 10, under continual stirring at 65°C for 1 h. Meanwhile, the color of the solution changed from white or brown (depending on the iron content) to milky white, which indicates the conversion of  $\text{Zn}^{2+}$  to  $\text{Zn}(\text{OH})_2$  according to Eq. (1) (Akir et al. 2016; Türkyılmaz et al. 2017). The resulting samples were centrifuged at 6500 rpm for 15 min and subsequently washed several times with deionized water to remove residual and unwanted impurities. Eventually, to convert the  $\text{Zn}(\text{OH})_2$  to ZnO (Eq. (2)), the precipitates were oven-dried at 100°C for 12 h. In this way, Fe-doped ZnO nanoparticles with different concentrations of  $\text{Fe}^{3+}$  (0, 1, 3, and 5 mol%) were prepared and denoted as PZ, FZ1, FZ3, and FZ5, respectively.



## Fabrication of Fe-doped ZnO/nanocellulose nanocomposite

An *in situ* technique was used for the fabrication of the Fe-doped ZnO/nanocellulose nanocomposite. For this purpose, 2.2 g of  $\text{Zn}(\text{CH}_3\text{CO}_2)_2 \cdot 2\text{H}_2\text{O}$  and 0.027 g of  $\text{FeCl}_3 \cdot 6\text{H}_2\text{O}$  (mole ratio 1:0.01) were dissolved in 50 ml of deionized water and then heated to 65°C under constant stirring. Afterwards, a specific amount of NC was added to the previous solution to obtain different NC/ $\text{Zn}^{2+}$  molar ratios (0.1, 0.2, 0.3, and 0.4) under constant stirring of 500 rpm for 1 h. Subsequently, the mixture was sonicated, using an ultrasonic water bath (Easy 30 H, Elma, Germany) for 1 h to achieve a homogenous blend. Then, about 50 ml of 1 M NaOH solution was added dropwise under constant stirring to attain pH 10. The samples were centrifuged and rinsed several times with distilled water to remove impurities. Finally, the product was oven-dried at 100°C for 12 h. The fabricated nanocomposites were labelled as CFZ1-1, CFZ1-2, CFZ1-3, and CFZ1-4 which represent different NC/ $\text{Zn}^{2+}$  molar ratios of 0.1, 0.2, 0.3, and 0.4, respectively.

## Sample characterization

The functional groups of BS, BBS, NC, PZ, FZs, and CFZs were characterized using an FTIR spectrometer (WQF-520, China). The crystalline phase and crystallite size of samples were determined by XRD spectroscopy using a Philips PW 1730 X-ray diffractometer with Cu radiation source ( $\lambda = 1.5406 \text{ \AA}$ ). The used accelerating voltage and tube current were 40 kV and 30 mA, respectively. The scanning of samples was recorded in the diffraction angle ( $2\theta$ ) range of  $5\text{-}80^\circ$ . The surface and structural morphology of the synthesized samples were analyzed by FESEM (TESCAN MIRA, Czech) and TEM (Philips CM120, Germany). The optical transmittance of PZ, FZs and CFZs was measured using UV-vis DRS (Shimadzu UV-160 A, China) in the range of 190-1100 nm. The thermal decomposition behavior of the samples was monitored by TGA and DTG analyses using a Mettler Toledo apparatus. The heating was carried out under  $N_2$  atmosphere at a flow rate of 200 mL/min and a heating rate of  $10^\circ\text{C}/\text{min}$  in the range of  $25\text{-}600^\circ\text{C}$ . The photocatalytic degradation of MB was determined by absorbance measurement using a UV-visible spectrophotometer (Unico 2800, USA) at 664 nm.

## Photocatalytic study

The photocatalytic performance of the samples was analyzed by investigating the degradation of MB as a model pollutant. A 6 W UVC lamp (254 nm) and a 250 W high-pressure mercury lamp equipped with a UV-cut filter ( $<400 \text{ nm}$ ) were used as UV and visible irradiation sources, respectively. In a typical photocatalytic experiment, 0.1 g of the sample (PZ, FZs, or CFZs) was added to 100 ml of 5 ppm MB solution. Then, the mixture was stirred and kept in a dark place prior to the photocatalytic reaction for 30 min to ensure the establishment of an adsorption and desorption equilibrium (Ali et al. 2021). Subsequently, the mixture was irradiated under UV or visible light for photodegradation of MB. During the reaction, aliquots were taken from the solution at regular intervals. To separate the catalyst from the solution, the samples were centrifuged at 6500 rpm for 30 min and the dye concentration was analyzed. The photocatalytic degradation efficiency of MB was calculated using Eq. (3).

$$\text{Degradation}\% = \frac{(C_0 - C_t)}{C_0} \times 100 \quad (3)$$

where,  $C_0$  is the initial dye concentration in the solution and  $C_t$  is the concentration of dye at any time. The influence of experimental parameters such as solution pH (3, 5, 7, 9, and 11), catalyst dosage (0.5, 1.0, 1.5, and 2.0 g/L), and initial MB concentration (5, 10, 15, 20, and 25 ppm) on its degradation by the best-performing catalyst was investigated. After photocatalytic reaction under the optimum condition, the nanocomposite was separated and washed with water for reuse in the next run of MB photodegradation under the same condition. The regeneration tests of the nanocomposite were done 4 times.

## Results And Discussions

### FTIR analysis

The FTIR spectra of BS, BBS, NC, PZ, FZ1, and CFZ1-2 were scanned in the range of 4000 – 400  $\text{cm}^{-1}$  and the recorded spectra are illustrated in Fig. 2. The broadbands observed at 3408  $\text{cm}^{-1}$  in all samples belong to the stretching vibration of O-H and the peak at 1646  $\text{cm}^{-1}$  is attributed to the absorbed water molecules by the samples (Langari et al. 2019). These peaks show the hydrophilic tendency of all samples. As shown in Fig. 3(a), the band located around 2894  $\text{cm}^{-1}$  is assigned to the C-H stretching vibration in cellulose structure (Lefatshe et al. 2017). The bands at 896 and around 1060  $\text{cm}^{-1}$  in all spectra are attributed to the C-H rocking and C-O stretching vibrations of cellulose, respectively (Chandra et al. 2016). In addition, the peak at 1160  $\text{cm}^{-1}$  is related to the stretching of C-O-C in the  $\beta$ -1,4-glycosidic linkages between D-glucose units in cellulose (Lee et al. 2017). The increase in the intensity of these peaks from BS to isolated NC shows the enhancement of the cellulose content. The peak observed at 1732  $\text{cm}^{-1}$  in the spectrum of BS is assigned to the presence of C=O stretching vibration of acetyl and carbonyl groups in hemicellulose or the ester linkage of carboxylic group in the ferulic and p-coumaric acids of lignin and/or hemicellulose (Lee et al. 2017). Additionally, the peaks at 1508 and 1254  $\text{cm}^{-1}$  are associated with the C=C and C-O stretching in aromatic skeletal vibrations of lignin, respectively. These peaks disappeared in the spectra of BBS and NC, indicating that the lignin content was decreased during bleaching and NC isolation (Chandra et al. 2016). The band at 1270  $\text{cm}^{-1}$  in the spectrum of BS is referred as the C-O stretching vibration of hemicellulose (Shahbazi et al. 2017). However, the reduction of this peak in the spectrum of BBS indicates the hemicellulose removal after bleaching. These results indicate that alkali and bleaching treatments were effective to extract highly purified cellulose. Moreover, the increase in the intensity of characteristic peaks of cellulose shows that the structure of cellulose was not degraded after alkali pretreatments, bleaching and acid hydrolysis (Shahbazi et al. 2017). The FTIR spectra of NC, PZ, FZ1, and CFZ1-2 are presented in Fig. 3(b). The characteristic peaks around 430-500  $\text{cm}^{-1}$  correspond to metal-oxygen vibration, which are observed in the spectra of PZ, FZ1 and CFZ1-2. It is worth noting that the characteristic peaks of FZ1 are similar to those of PZ, indicating that the doped Fe into ZnO existed in the form of elements. Similar characteristic peaks of NC were observed in the spectrum of CFZ1-2 composite. Moreover, compared with NC, a new absorption peak at 400–500  $\text{cm}^{-1}$  assigned to Zn-O or Fe -O stretching vibration was found in the CFZ1-2 composite (Guan et al. 2019). Furthermore, it could be seen that the intensity of these characteristic peaks decreased in the spectrum of CFZ1-2. This reduction confirms the strong interaction between FZ particles and NC chains.

## Morphology and dimensions

Figure 3. displays the FESEM and TEM images of as-prepared samples. As shown in Figs. 3(a<sub>1</sub>-a<sub>3</sub>), before alkali pretreatment and bleaching, the BS showed a rigid uniform structure and the fibers of the BS were fully cemented with hemicellulose and lignin. Importantly, the surface of samples was rough, probably due to the presence of lignin. However, after alkali treatment and bleaching, the BS fibers exhibited a loose structure due to the degradation of lignin and hemicellulose removal. After ultrasonic-assisted acid hydrolysis, the obtained NC revealed nearly spherical nanostructure with an average particle diameter of 70 nm (Figure 3(a<sub>3</sub>)).

Figures 3(b<sub>1</sub>-b<sub>4</sub>) show the surface morphologies of the pristine and Fe-doped ZnO. As shown in the FESEM images, the average size of the particles was in the nanometer range. It is evident from Fig. 3(b<sub>1</sub>) that PZ sample presented a nearly zero-dimensional (0D) growth with the diameter of 100 nm and Fe<sup>3+</sup> doping affected the growth direction and the shape of the synthesized nanoparticles. In the FZ1, FZ3, and FZ5 samples, the 0D growth of PZ gradually turned into 1D growth and the particle length increased to 120±10, 140±10, and 150±10 nm, respectively. The particle diameter was slightly influenced by the dopant concentration. As the dopant concentration increased from 1 to 5%, the diameter decreased from 50±10 to 30±10 nm. The surface morphology of CFZ hybrid nanocomposites is shown in Figures 3(c<sub>1</sub>-c<sub>4</sub>). As can be seen, by the addition of NC during the synthesis of FZ1, the average diameter of nanocomposite increased to 70±10, 75±10, 85±10, and 100±10 nm for CFZ1-1, CFZ1-2, CFZ1-3, and CFZ1-4 samples, respectively. Besides, due to the greater tendency of NC to form a precipitate, with increasing its content in the nanocomposite, larger sediments were observed in the nanocomposites.

Figures 3(d<sub>1</sub>-d<sub>4</sub>) display the TEM images of NC, PZ, FZ1, and CFZ1-2, respectively. The image of the NC sample clearly revealed that the particle size distribution of NC was in the range of 20 to 150 nm which were scattered next to each other (Fig. 3(d<sub>1</sub>)). The TEM image of PZ sample evidently exhibited the spherical morphology of the nanoparticles (Fig. 3(d<sub>2</sub>)). It is clear that Fe<sup>3+</sup> doping changed the morphology of the PZ particles (Fig. 3(d<sub>3</sub>)). Further, the TEM image of CFZ1-2 composite illustrated in Fig. 3d<sub>4</sub> identifies that particles were fabricated with successful integration between Fe-ZnO and NC.

## XRD analysis

The XRD analysis was carried out to identify the crystalline structure of samples. The diffraction patterns of the BS and NC samples are shown in Fig. 4a. The patterns of both samples exhibited typical cellulose I peak around  $2\theta = 16.1^\circ$ ,  $22.5^\circ$ , and  $34.1^\circ$  attributed to (110), (200), and (004) planes, respectively (Abdalkarim et al. 2018; French 2014). The crystallinity index (CI) is an important parameter that influences the physical and mechanical properties of cellulose. From the XRD profiles, the CI of BS and NC was calculated using the Segal equation as follows (Gedik 2021):

$$CI\% = \frac{I_{mi} - I_{am}}{I_{mi}} \times 100 \quad (4)$$

where  $I_{mi}$  is the maximum intensity of the principal peak (200) and  $I_{am}$  is the value of the intensity minimum of the peak (110) at  $2\theta = 16.1^\circ$ , which represents the amorphous fraction. The calculated CI was 40.27 and 60.16% for the BS and NC, respectively. According to the results, it was found that the treatment steps affected the crystallinity of the BS by the removal of excess amorphous regions, such as lignin, hemicellulose, and the amorphous region of cellulose from the BS fibers.

The XRD patterns of PZ and FZs are shown in Figs. 4(b-c). As shown in the XRD patterns, PZ and FZs samples displayed many intense peaks at  $2\theta = 31.78^\circ$ ,  $34.41^\circ$ ,  $36.25^\circ$ ,  $47.53^\circ$ ,  $56.59^\circ$ ,  $62.83^\circ$ ,  $66.39^\circ$ ,  $67.64^\circ$ ,  $69.05^\circ$ ,  $72.53^\circ$ , and  $76.92^\circ$  which assigned to the (100), (002), (101), (102), (110), (103), (200),

(112), (201), (004), and (202) planes of the hexagonal wurtzite structure, respectively, and resemble those previously reported (Isai and Shrivastava 2019). On the basis of wurtzite structure, the PZ and FZs samples correspond to the standard data (JCPDS No.01-080-0074). Meanwhile, no additional peaks were detected in FZs patterns, which indicated that iron was well doped into the crystal phase of PZ. The XRD diffractograms of CFZs nanocomposite are illustrated in Fig. 4(d). The CFZs patterns exhibited two-phase structures corresponding to FZ and NC. It can be deduced that the presence of NC did not alter the crystal structure of FZ, and Fe-doped ZnO was crystallized well in the NC polymeric matrix, as no new peaks were detected.

The average crystallite size (D) of the PZ, FZs and CFZs was calculated using the Scherrer formula as:

$$D = \frac{0.89\lambda}{\beta \cos \theta} \quad (5)$$

where  $\lambda$  is the wavelength of the X-ray radiation (0.15406 nm),  $\beta$  is the full width at half maximum (FWHM) measured in radians, and  $\theta$  is the Bragg diffraction angle.

The (110) peak, the most intense peak for PZ, FZs, and CFZs samples, was used for the calculation of the crystallite sizes. The calculated crystallite size for PZ, FZs, and CFZs is summarized in Table 2. The average crystallite size of PZ was 17.8 nm. Results showed that the Fe-doped ZnO nanoparticles with higher content of Fe revealed smaller average crystallite sizes. Results showed that the substitution of  $\text{Fe}^{3+}$  (0.64 Å) in place of  $\text{Zn}^{2+}$  (0.74 Å) in zinc oxide lattice reduced the growth rate of zinc oxide crystallites as observed in other studies (Ciciliati et al. 2015; Saleh et al. 2012; Xiao, Zhang, Wei, and Chen 2018). The average crystallite size of CFZ1-1, CFZ1-2, CFZ1-3, and CFZ1-4 was 12.7, 11.0, 9.1, and 8.2 nm, respectively. Compared to the crystallite size of FZ1, the crystallite size of CFZs reduced which is due to the inhibition of NC from the nucleation and growth of ZnO nanocrystals (Fabbiyola et al. 2016). The NC as a matrix could disperse Fe-doped ZnO particles and further decrease the crystallite size of Fe-doped ZnO.

Table 3  
The calculated average crystallite size of PZ, FZs, and CFZs

Samples	Composition	Average crystallite size (nm)
PZ	Pure ZnO	17.8
FZ1	1% Fe doped ZnO	15.5
FZ3	3% Fe doped ZnO	14.4
FZ5	5% Fe doped ZnO	13.6
CFZ1-1	1% Fe doped + 0.1 NC blended ZnO	12.7
CFZ1-2	1% Fe doped + 0.2 NC blended ZnO	11.0
CFZ1-3	1% Fe doped + 0.3 NC blended ZnO	9.1
CFZ1-4	1% Fe doped + 0.4 NC blended ZnO	8.2

# UV-vis DRS analysis and bandgap study

The influence of  $\text{Fe}^{3+}$  doping on optical properties of ZnO was studied using UV–vis DRS analysis. The diffuse reflectance spectra of the pure ZnO and FZs are displayed in Fig. 5(a). It was observed that the pristine ZnO nanoparticles exhibited a low diffuse reflectance at wavelengths less than 400 nm, which corresponds to an intense absorption peak between 200 to 400 nm. This result indicates that the PZ can efficiently absorb UV light. Compared to the pure ZnO, the FZs samples had lower diffuse reflectance in the visible region. On the other hand, Fe-doped samples were able to efficiently absorb visible light (solar light) for the photocatalytic process. Additionally, the bandgap energy of all samples was calculated from the well-known Kubelka-Munk (KM) equation and the plots are illustrated in Fig. 5(b). The calculated bandgap energy of the FZ1, FZ3 and FZ5 samples are approximately 3.09, 3.03, and 3.01 eV, respectively, which is smaller than that of PZ (3.22 eV). This reduction could be attributed to the *s-d* and *p-d* exchange interactions between the band electrons and the d electrons of the  $\text{Fe}^{3+}$  ions substituting  $\text{Zn}^{2+}$  ions (Ciciliati et al. 2015).

## Thermal stability

The TGA and DTG curves of NC, PZ, FZ1, and CFZ1-2 samples are depicted in Fig. 6. The PZ sample exhibited approximately 2.0% initial weight loss below 100°C, which corresponds to the evaporation of the adsorbed water on the surface of PZ nanoparticles. Then, subsequent weight loss of 4.3% occurred at 260-320°C, which was attributed to the removal of organic components. The FZ1 sample displayed the highest thermally stability. A total weight loss of 2.6% was found for FZ1 sample. As observed, the thermal degradation of NC and CFZ1-2 samples took place in two stages. The first weight loss of 5% for NC sample occurred at about 250°C; this was followed by a second weight loss of 60%, which happened at around 330°C. The thermal weight loss of NC during this stage was mainly attributed to the depolymerization, dehydration, and decomposition of glycosyl units of NC sample. Compared with the NC sample, the thermal degradation peaks for CFZ1-2 were found at higher temperatures (290 and 350°C). This was related to the stronger interactions between oxygen atoms of the NC and FZ1 nanoparticles that provide a thermal barrier for the NC skeleton. The TGA analysis showed a total weight loss of 22.76% for CFZ1-2. These results indicate that the thermal stability of CFZ1-2 was better than that of NC.

## Photocatalytic degradation of MB

The photocatalytic activity of PZ and FZs was investigated in the MB degradation reaction, when exposed to both UV and visible light irradiations. In these experiments, the effect of iron ions in the photocatalysts on the degradation of MB was evaluated. In order to minimize the influence of adsorption of the synthesized catalyst, each experiment was performed in the dark condition for 30 min prior to the light irradiation. Fig. 7(a) shows the photocatalytic degradation of MB in an aqueous solution with PZ and FZs nanoparticles under UV light radiation. It can be observed that the PZ sample degraded 93.13% of the MB dye in 150 min under UV light radiation, but the prepared Fe-doped samples exhibited lower photocatalytic activity. As the dopant molar ratio increased from 1 to 3 and 5%, the degradation of MB correspondingly decreased from 86.34 to 73.81 and 66.25%, respectively. As shown in Fig. 7(b), under UV

light irradiation, the Fe ions in the ZnO crystal structure act as an electron-hole trap and promote the charge recombination. Thus, increasing the Fe dopant ratio reduces the photocatalyst activity by disrupting the redox process.

Figure 8(a) illustrates the photocatalytic degradation of MB in an aqueous solution with PZ and FZs nanoparticles under visible light radiation. The degradation efficiency of MB over the PZ catalyst was 39.96% in 150 min of visible light irradiation. The pristine ZnO revealed poor photocatalytic performance under visible light irradiation compared to that under UV light irradiation. This could be attributed to the high bandgap of ZnO. As observed in Figure 8(a), the FZ1 catalyst exhibited the highest degradation efficiency of MB (94.21%), followed by FZ2 (83.97%) and FZ3 (50.62%). As expected, the increase of Fe<sup>3+</sup> doping ratio was very effective to enhance the performance of ZnO. A number of researches confirmed that the photocatalytic degradation efficiency of ZnO can be enhanced by doping with iron ions (Xiao, Zhang, Wei, Yu, et al. 2018; Yi et al. 2014). A scheme of plausible mechanism for the MB photocatalytic degradation over Fe-doped ZnO under visible light is displayed in Figure 8(b). According to the previous studies (Yi et al. 2014), the photodegradation of dye under visible light irradiation is not due to the direct reaction between photogenerated electron holes on the surface of catalyst and dye, but can be attributed to the photosensitization effect of the dye molecules. During this process, the MB molecules could absorb visible light in the range 450-600 nm and get excited by the visible light. Then, the electrons on the highest occupied molecular orbital (HOMO) of MB molecules transfer to the lowest unoccupied molecular orbital (LUMO) and are immediately injected to the conduction band (CB) of ZnO, whereas MB is converted to its radicals (MB•+) form. When iron ions are added into the ZnO structure, they could increase the electron capture capacity of ZnO from the photosensitizer (MB). This process could absorb more photons and effectively enhance the separation of the electron-hole pairs. The transferred electrons to the CB could react with electron acceptors such as the adsorbed O<sub>2</sub> on the surface of the catalyst to make superoxide radical anion O<sub>2</sub><sup>•-</sup>, which are further converted to HO<sup>•</sup>, H<sub>2</sub>O<sub>2</sub> and HO<sup>•</sup> species via a series of reactions. However, when the doping ratio was 3 and 5%, the formed ZnFe<sub>2</sub>O<sub>4</sub> occupies the active sites and hinders the electrons transfer to Fe<sup>3+</sup>; thus, the electron-hole pairs could not be separated effectively, so the photocatalytic activity is gradually reduced to 83.97 and 50.62% for FZ3 and FZ5, respectively (Türkyılmaz et al. 2017; Yi et al. 2014).

The prepared CFZ samples were also utilized to evaluate their dye removal performance; the results of this investigation are exhibited in Fig. 9(a). Results showed that the dye removal at the dark condition was influenced by the NC content in nanocomposite. The dye removal increased with an increase in NC /Zn<sup>2+</sup> molar ratio from 0.1 to 0.4. The possible mechanism of MB degradation during this time is physical adsorption that relies on the surface hydroxyl or sulfate ester groups of NC and electrostatic attraction between NC and MB (An et al. 2020). MB is a positively charged cationic dye, while the surface charge of CFZs was negative; this could form a strong electrostatic interaction between them. The dye removal efficiency of CFZ1-1, CFZ1-2, CFZ1-3, and CFZ1-4 at the end of the dark time was 25.53, 33.99, 40.09 and 51.33%, respectively. Compared to other nanocomposites, CFZ1-4 with a higher molar ratio of NC to Zn<sup>2+</sup> showed the highest dye removal efficiency. The photocatalytic activity of CFZs was

evaluated for MB degradation under visible light. It can be observed that the CFZ samples possessed photocatalytic ability to degrade the MB under visible light irradiation. Based on the obtained results, the performance of CFZ1-1 with a degradation efficiency of 86.61% was weaker than that of CFZ1-2 with 97.81% degradation efficiency, which was probably related to the incomplete incorporation of NC in photocatalyst particles in the CFZ1-1 sample. With further increase in the molar ratio of NC to  $Zn^{+2}$  from 0.2 to 0.4, there was a reduction in the degradation efficiency. This might be due to the low absorption of light by NC and the coverage of photocatalytic particles by this biopolymer which limited the photocatalytic activity of these particles. The degradation efficiency of CFZ1-3 and CFZ1-4 was 69.34 and 54.34%, respectively, which was lower than that of CFZ1-2. According to the results, the multifunctional CFZ1-2 sample showed the best combination of adsorption and photocatalytic activity among the PZ, FZs, and CFZs samples. Therefore, CFZ1-2 was used to study its photocatalytic performance for the degradation of MB in the subsequent experiments.

## Effect Of Solution Ph

As reported in several studies, adsorption facilitates the photocatalytic degradation process; higher adsorption results in a greater effectiveness of the photocatalysis process (Kumar et al. 2018; Tran et al. 2021). The dye molecules adsorbed on the catalyst surface are degraded faster than those in bulk due to the short life and easy annihilation of charge carriers or reactive radicals during diffusion or migration (Tran et al. 2021). By influencing the charging behavior of the catalyst and dye, the pH of the solution is an important factor that affects the dye photocatalytic degradation. The concentration of hydroxyl radicals, charge of the molecule, adsorption/desorption of the dye molecule and its intermediates onto a photocatalyst surface, and the surface charge property of the photocatalyst depend upon the pH of the dye solution. In order to determine the surface charge of CFZ1-2, the pH of zero-point charge ( $pH_{pzc}$ ) was determined (data not shown). It was obtained to be 8.1, which indicates that the surface charge of the catalyst is positive when  $pH < 8.1$  and vice versa. The solution pH was varied from 3 to 11 to study its effect on the photocatalytic degradation of the MB dye. Fig. 10 (a) indicates the effect of solution pH on the MB degradation. Results revealed that CFZ1-2 could act effectively over a wide range of pH (from 3 to 11). As expected, CFZ1-2 exhibited the highest degradation performance at pH 9, followed by pH 11, 7, 5, and 3. At acidic pH, the degradation of MB was unfavorable due to the strong electrostatic repulsion between CFZ1-2 and MB molecules. Besides, the acidic condition could increase the competitive adsorption of  $H^+$  with MB, hindering the MB access to the catalyst surface. The high degradation of MB may be resulted from the electrostatic attraction between the negative surface charge of CFZ1-2 and the positive charge of cationic dye (MB), while the pH of the solution was above the  $pH_{pzc}$  (8.1). Thus, pH 9 was selected as the optimum pH for MB degradation.

### Effect of nanocomposite dosage

The effect of catalyst dosage on MB degradation efficiency was studied with different amounts of CFZ1-2 (0.5 to 2.0 g/L) after 90 min irradiation under visible light. As shown in Fig. 10 (b), the degradation

efficiency enhanced with raising the catalyst dosage up to 1.5 g/L and reduced thereafter. An explanation for the observed trend could be attributed to the number of active sites on the catalyst, which enhanced with the addition of the photocatalyst, improving the degradation efficiency. However, an increase of the catalyst dosage to over 1.5 g/L had negative effect on the catalyst performance and led to the reduction of the degradation efficiency of CFZ1-2. It seems that the enhancement of catalyst amounts could lead to the agglomeration of photocatalyst particles, light scattering, and hindering the light transmission, hindering the photocatalytic performance (Emadian et al. 2020; Mirzaeifard et al. 2020). Based on the results, the optimum dosage of CFZ1-2 for MB degradation was selected at 1.5 g/L for the subsequent experiments.

### **Effect of initial dye concentration**

The influence of initial dye concentration (5-25 ppm) on dye degradation by 1.5 g/L of the CFZ1-2 photocatalyst at pH= 9 was studied. As can be observed in Fig. 10(c), by increasing the dye concentration, the photocatalytic degradation indicated a downward trend. At a constant amount of catalyst, the number of active sites in the catalyst reduced upon dye adsorption onto the surface of catalyst, resulting in a decrease in the active radical production and also reduction of degradation of efficiency. Furthermore, when the MB concentration was increased, the turbidity of reaction mixture also increased that acted as a screen against visible light, prevented the light photons from reaching the active sites of the catalyst and deteriorated the photocatalytic degradation (Raja et al. 2020).

### **Regeneration**

The reusability and stability of a photocatalyst are critical parameters for its practical application. The reusability of the CFZ1-2 as optimal photocatalyst was investigated under optimized conditions for the MB degradation (pH=9, catalyst dosage= 1.5 g/L, and MB initial concentration=5 ppm). The reusability tests were done by centrifuging the CFZ1-2 nanocomposite sample from the first cycle, which was then washed and oven-dried at 50°C. Fig. 11 illustrates that the degradation efficiency of the CFZ1-2 sample slightly decreased from 98.84 to 97.51, 95.39, 94.11, and 92.31% during the different reuse runs. In fact, the degradation efficiency of CFZ1-2 was kept higher than 92% after five successive runs. This negligible reduction of degradation efficiency might be attributed to the trapping of MB molecules on the active sites of the catalyst surface and the loss of the catalyst throughout the cycling experiments. The obtained result confirms that the synthesized photocatalyst is a promising catalyst for long-term uses in industrial wastewater treatment processes.

## **Conclusion**

In this study, NC was successfully isolated from broomcorn stalk, characterized and used to prepare CNC/Fe-doped ZnO nanocomposite through a facile *in-situ* method. The fabricated samples were characterized by various techniques and used for the degradation of MB. The comparison of PZ and FZs photocatalytic performance in the presence of visible light showed that the presence of Fe<sup>3+</sup> in ZnO

matrix effectively increased the ZnO photocatalytic performance. The degradation efficiency of FZ1 was about 94.21% at 150 min that was higher than that of PZ (36.96%) in the same duration. The higher degradation efficiency of FZ1 could be related to the decreased bandgap of Fe-doped ZnO compared to pure ZnO that led to enhanced absorbance of photons under the visible light and inhibited the recombination of electron/hole pairs. Compared with PZ and FZs, the synthesized CFZs indicated superior photocatalytic performance. The photocatalytic performance of CFZ1-2 was evaluated at different pH, photocatalyst dosages, and initial MB concentrations. It was observed that a maximum MB degradation of 98.84% was achieved by 15 g/L CFZ1-2 in 5 ppm MB solution at pH=9 in 90 min under visible irradiation. The photocatalytic efficiency of the CFZ1-2 was examined up to five cycles and the catalyst was able to preserve its original performance with more than 92% degradation efficiency even on reuse. Hence, CFZ1-2 can be regarded as a great photocatalyst nanocomposite for the enhanced degradation of cationic dye impurities under visible light irradiation.

## Declarations

## Conflicts of interest

We declare we have no competing interests.

## Acknowledgment

This work was supported by Babol Noshirvani University of Technology (BNUT) through the postgraduate student grant BNUT/964115043/1400.

## References

1. Abad S N K, Mozammel M, Moghaddam J et al (2020) Highly porous, flexible and robust cellulose acetate/Au/ZnO as a hybrid photocatalyst. *Appl. Surf. Sci.* 526:146237. <https://doi.org/10.1016/j.apsusc.2020.146237>
2. Abdalkarim S Y H, Yu H-Y, Wang C et al (2018) Green synthesis of sheet-like cellulose nanocrystal–zinc oxide nanohybrids with multifunctional performance through one-step hydrothermal method. *Cellulose* 25:6433-46. <https://doi.org/10.1007/s10570-018-2011-0>
3. Abdel-Wahab M S, Jilani A, Yahia I et al (2016) Enhanced the photocatalytic activity of Ni-doped ZnO thin films: Morphological, optical and XPS analysis. *Superlattices Microstruct.* 94:108-18. <https://doi.org/10.1016/j.spmi.2016.03.043>
4. Abebe B, HC A M, Zerefa E et al (2020) Porous PVA/Zn–Fe–Mn oxide nanocomposites: methylene blue dye adsorption studies. *Mater. Res. Express* 7:065002. <https://doi.org/10.1088/2053-1591/ab94fc>

5. Akir S, Barras A, Coffinier Y et al (2016) Eco-friendly synthesis of ZnO nanoparticles with different morphologies and their visible light photocatalytic performance for the degradation of Rhodamine B. *Ceram* 42:10259-65. <https://doi.org/10.1016/j.ceramint.2016.03.153>
6. Ali A, Shoeb M, Li Y et al (2021) Enhanced photocatalytic degradation of antibiotic drug and dye pollutants by graphene-ordered mesoporous silica (SBA 15)/TiO<sub>2</sub> nanocomposite under visible-light irradiation. *J. Mol. Liq.* 324:114696. <https://doi.org/10.1016/j.molliq.2020.114696>
7. An V N, Van T T, and Nhan H T (2020) Investigating Methylene Blue Adsorption and Photocatalytic Activity of ZnO/CNC Nanohybrids. *J. Nanomater.* 2020. <https://doi.org/10.1155/2020/6185976>
8. Ba-Abbad M M, Kadhum A A H, Mohamad A B et al (2013) Visible light photocatalytic activity of Fe<sup>3+</sup>-doped ZnO nanoparticle prepared via sol–gel technique. *Chemosphere* 91:1604-11. <https://doi.org/10.1016/j.chemosphere.2012.12.055>
9. Chand P, Singh V, and Kumar D (2020) Rapid visible light-driven photocatalytic degradation using Ce-doped ZnO nanocatalysts. *Vacuum* 178:109364. <https://doi.org/10.1016/j.vacuum.2020.109364>
10. Chandra J, George N, and Narayanankutty S K (2016) Isolation and characterization of cellulose nanofibrils from arecanut husk fibre. *Carbohydr. Polym.* 142:158-66. <https://doi.org/10.1016/j.carbpol.2016.01.015>
11. Ciciliati M A, Silva M F, Fernandes D M et al (2015) Fe-doped ZnO nanoparticles: Synthesis by a modified sol–gel method and characterization. *Mater. Lett.* 159:84-86. <https://doi.org/10.1016/j.matlet.2015.06.023>
12. Elfeky A S, Salem S S, Elzaref A S et al (2020) Multifunctional cellulose nanocrystal/metal oxide hybrid, photo-degradation, antibacterial and larvicidal activities. *Carbohydr. Polym.* 230:115711. <https://doi.org/10.1016/j.carbpol.2019.115711>
13. Emadian S S, Ghorbani M, and Bakeri G (2020) Magnetically separable CoFe<sub>2</sub>O<sub>4</sub>/ZrO<sub>2</sub> nanocomposite for the photocatalytic reduction of hexavalent chromium under visible light irradiation. *Synth. Met.* 267:116470. <https://doi.org/10.1016/j.synthmet.2020.116470>
14. Evdokimova O, Fedulova A, Evdokimova A et al (2020) Preparation of Hybrid Nanocomposites Based on Nanoscale Cellulose and Magnetic Nanoparticles with Photocatalytic Properties. *Inorg. Mater. Appl. Res.* 11:371-76. <https://doi.org/10.1134/S2075113320020100>
15. Fabbiyola S, Kennedy L J, Ratnaji T et al (2016) Effect of Fe-doping on the structural, optical and magnetic properties of ZnO nanostructures synthesised by co-precipitation method. *Ceram* 42:1588-96. <https://doi.org/10.1016/j.ceramint.2015.09.110>
16. Flores K, Valdes C, Ramirez D et al (2020) The effect of hybrid zinc oxide/graphene oxide (ZnO/GO) nano-catalysts on the photocatalytic degradation of simazine. *Chemosphere* 259:127414. <https://doi.org/10.1016/j.chemosphere.2020.127414>
17. French A D (2014) Idealized powder diffraction patterns for cellulose polymorphs. *Cellulose* 21:885-96. <https://doi.org/10.1007/s10570-013-0030-4>
18. Fu F, Gu J, Xu X et al (2017) Interfacial assembly of ZnO–cellulose nanocomposite films via a solution process: a one-step biomimetic approach and excellent photocatalytic properties. *Cellulose*

- 24:147-62. <https://doi.org/10.1007/s10570-016-1087-7>
19. Ganguly K, and Lim K-T (2020) Nanocellulose-based polymer nanohybrids and nanocomposite applications. in, *Multifunctional Hybrid Nanomaterials for Sustainable Agri-Food and Ecosystems* (Elsevier). <https://doi.org/10.1016/B978-0-12-821354-4.00020-0>
  20. Gedik G (2021) Extraction of new natural cellulosic fiber from *Trachelospermum jasminoides* (star jasmine) and its characterization for textile and composite uses. *Cellulose*:1-17. <https://doi.org/10.1007/s10570-021-03952-1>
  21. Guan Y, Yu H-Y, Abdalkarim S Y H et al (2019) Green one-step synthesis of ZnO/cellulose nanocrystal hybrids with modulated morphologies and superfast absorption of cationic dyes. *Int. J. Biol. Macromol.* 132:51-62. <https://doi.org/10.1016/j.ijbiomac.2019.03.104>
  22. Isai K A, and Shrivastava V S (2019) Photocatalytic degradation of methylene blue using ZnO and 2% Fe–ZnO semiconductor nanomaterials synthesized by sol–gel method: a comparative study. *SN Appl. Sci.* 1:1-11. <https://doi.org/10.1007/s42452-019-1279-5>
  23. Jiang Y, Lawan I, Zhou W et al (2020) Synthesis, properties and photocatalytic activity of a semiconductor/cellulose composite for dye degradation-a review. *Cellulose* 27:595-609. <https://doi.org/10.1007/s10570-019-02851-w>
  24. Kamal T, Ul-Islam M, Khan S B et al (2015) Adsorption and photocatalyst assisted dye removal and bactericidal performance of ZnO/chitosan coating layer. *Int. J. Biol. Macromol.* 81:584-90. <https://doi.org/10.1016/j.ijbiomac.2015.08.060>
  25. Kim D, and Yong K (2021) Boron doping induced charge transfer switching of a C<sub>3</sub>N<sub>4</sub>/ZnO photocatalyst from Z-scheme to type II to enhance photocatalytic hydrogen production. *Appl. Catal. B* 282:119538. <https://doi.org/10.1016/j.apcatb.2020.119538>
  26. Kumar A, Kumar A, Sharma G et al (2018) Quaternary magnetic BiOCl/g-C<sub>3</sub>N<sub>4</sub>/Cu<sub>2</sub>O/Fe<sub>3</sub>O<sub>4</sub> nano-junction for visible light and solar powered degradation of sulfamethoxazole from aqueous environment. *Chem. Eng. Sci.* 334:462-78. <https://doi.org/10.1016/j.ces.2017.10.049>
  27. Kumar S G, and Rao K K (2015) Zinc oxide based photocatalysis: tailoring surface-bulk structure and related interfacial charge carrier dynamics for better environmental applications. *RSC Adv.* 5:3306-51. <https://doi.org/10.1039/C4RA13299H>
  28. Langari M M, Nikzad M, Ghoreyshi A A et al (2019) Isolation of nanocellulose from broomcorn stalks and its application for nanocellulose/xanthan film preparation. *ChemistrySelect* 4:11987-94. <https://doi.org/10.1002/slct.201902533>
  29. Lavand A B, and Malghe Y S (2018) Synthesis, characterization and visible light photocatalytic activity of carbon and iron modified ZnO. *J. King Saud Univ. Sci.* 30:65-74. <https://doi.org/10.1016/j.jksus.2016.08.009>
  30. Lee B-M, Jeun J-P, Kang P-H et al (2017) Isolation and characterization of nanocrystalline cellulose from different precursor materials. *Fibers Polym.* 18:272-77. <https://doi.org/10.1007/s12221-017-6548-6>

31. Lefatshe K, Muiva C M, and Kebaabetswe L P (2017) Extraction of nanocellulose and in-situ casting of ZnO/cellulose nanocomposite with enhanced photocatalytic and antibacterial activity. *Carbohydr. Polym.* 164:301-08. <https://doi.org/10.1016/j.carbpol.2017.02.020>
32. Li H, Zhang L, Lu H et al (2020) Macro-/nanoporous Al-doped ZnO/cellulose composites based on tunable cellulose fiber sizes for enhancing photocatalytic properties. *Carbohydr. Polym.* 250:116873. <https://doi.org/10.1016/j.carbpol.2020.116873>
33. Li X, Zhang L, Wang Z et al (2021) Cellulose controlled zinc oxide nanoparticles with adjustable morphology and their photocatalytic performances. *Carbohydr. Polym.* 259:117752. <https://doi.org/10.1016/j.carbpol.2021.117752>
34. Lizundia E, Goikuria U, Vilas J L et al (2018) Metal nanoparticles embedded in cellulose nanocrystal based films: Material properties and post-use analysis. *Biomacromolecules* 19:2618-28. <https://doi.org/10.1021/acs.biomac.8b00243>
35. Masoudnia S, Juybari M H, Mehrabian R Z et al (2020) Efficient dye removal from wastewater by functionalized macromolecule chitosan-SBA-15 nanofibers for biological approaches. *Int. J. Biol. Macromol.* 165:118-30. <https://doi.org/10.1016/j.ijbiomac.2020.09.158>
36. Mirzaeifard Z, Shariatinia Z, Jourshabani M et al (2020) ZnO photocatalyst revisited: Effective photocatalytic degradation of emerging contaminants using S-doped ZnO nanoparticles under visible light radiation. *Ind. Eng. Chem. Res.* 59:15894-911. <https://doi.org/10.1021/acs.iecr.0c03192>
37. Moon R J, Martini A, Nairn J et al (2011) Cellulose nanomaterials review: structure, properties and nanocomposites. *Chem. Soc. Rev.* 40:3941-94. <https://doi.org/10.1039/C0CS00108B>
38. Muniyasamy A, Sivaporul G, Gopinath A et al (2020) Process development for the degradation of textile azo dyes (mono-, di-, poly-) by advanced oxidation process-Ozonation: Experimental & partial derivative modelling approach. *J. Environ. Manage.* 265:110397. <https://doi.org/10.1016/j.jenvman.2020.110397>
39. Nagaraju P, Puttaiah S H, Wantala K et al (2020) Preparation of modified ZnO nanoparticles for photocatalytic degradation of chlorobenzene. *Appl. Water Sci.* 10:1-15. <https://doi.org/10.1007/s13201-020-01228-w>
40. Namini A S, Delbari S A, Mousavi M et al (2021) Synthesis and characterization of novel ZnO/NiCr<sub>2</sub>O<sub>4</sub> nanocomposite for water purification by degradation of tetracycline and phenol under visible light irradiation. *Mater. Res. Bull.* 139:111247. <https://doi.org/10.1016/j.materresbull.2021.111247>
41. Qi K, Cheng B, Yu J et al (2017) Review on the improvement of the photocatalytic and antibacterial activities of ZnO. *J. Alloys Compd.* 727:792-820. <https://doi.org/10.1016/j.jallcom.2017.08.142>
42. Qi K, Xing X, Zada A et al (2020) Transition metal doped ZnO nanoparticles with enhanced photocatalytic and antibacterial performances: experimental and DFT studies. *Ceram* 46:1494-502. <https://doi.org/10.1016/j.ceramint.2019.09.116>
43. Raja A, Rajasekaran P, Selvakumar K et al (2020) Visible active reduced graphene oxide-BiVO<sub>4</sub>-ZnO ternary photocatalyst for efficient removal of ciprofloxacin. *Sep. Purif. Technol.* 233:115996.

- <https://doi.org/10.1016/j.seppur.2019.115996>
44. Rajendran S, Naushad M, Ponce L C et al (2020) Green Photocatalysts for Energy and Environmental Process. (Springer). <https://doi.org/10.1007/978-3-030-17638-9>
  45. Saffari R, Shariatnia Z, and Jourshabani M (2020) Synthesis and photocatalytic degradation activities of phosphorus containing ZnO microparticles under visible light irradiation for water treatment applications. *Environ. Pollut.* 259:113902. <https://doi.org/10.1016/j.envpol.2019.113902>
  46. Saleh R, Prakoso S P, and Fishli A (2012) The influence of Fe doping on the structural, magnetic and optical properties of nanocrystalline ZnO particles. *J. Magn. Magn.* 324:665-70. <https://doi.org/10.1016/j.jmmm.2011.07.059>
  47. Saxena M, Sharma N, and Saxena R (2020) Highly efficient and rapid removal of a toxic dye: Adsorption kinetics, isotherm, and mechanism studies on functionalized multiwalled carbon nanotubes. *Surf. Interfaces* 21:100639. <https://doi.org/10.1016/j.surfin.2020.100639>
  48. Shahbazi P, Behzad T, and Heidarian P (2017) Isolation of cellulose nanofibers from poplar wood and wheat straw: optimization of bleaching step parameters in a chemo-mechanical process by experimental design. *Wood Sci. Technol.* 51:1173-87. <https://doi.org/10.1007/s00226-017-0929-2>
  49. Shahbazkhany S, Salehi M, and Mousavi-Kamazani M (2020) Facile synthesis, characterization, and decolorization activity of Mn<sup>2+</sup> and Al<sup>3+</sup> co-doped hexagonal-like ZnO nanostructures as photocatalysts. *Appl. Organomet. Chem.* 34:e5346. <https://doi.org/10.1002/aoc.5346>
  50. Sharma M, Poddar M, Gupta Y et al (2020) Solar light assisted degradation of dyes and adsorption of heavy metal ions from water by CuO–ZnO tetrapodal hybrid nanocomposite. *Mater. Today Chem.* 17:100336. <https://doi.org/10.1016/j.mtchem.2020.100336>
  51. Sirajudheen P, Karthikeyan P, Vigneshwaran S et al (2020) Synthesis and characterization of La (III) supported carboxymethylcellulose-clay composite for toxic dyes removal: Evaluation of adsorption kinetics, isotherms and thermodynamics. *Int. J. Biol. Macromol.* 161:1117-26. <https://doi.org/10.1016/j.ijbiomac.2020.06.103>
  52. Sluiter A, Hames B, Ruiz R et al (2008) Determination of structural carbohydrates and lignin in biomass. *Laboratory analytical procedure* 1617:1-16.
  53. Tran V A, Nguyen T L H, and Doan V-D (2021) Fabrication of Fe<sub>3</sub>O<sub>4</sub>/CuO@ C composite from MOF-based materials as an efficient and magnetically separable photocatalyst for degradation of ciprofloxacin antibiotic. *Chemosphere* 270:129417. <https://doi.org/10.1016/j.chemosphere.2020.129417>
  54. Türkyılmaz Ş Ş, Güy N, and Özacar M (2017) Photocatalytic efficiencies of Ni, Mn, Fe and Ag doped ZnO nanostructures synthesized by hydrothermal method: The synergistic/antagonistic effect between ZnO and metals. *J. Photochem. Photobiol.* 341:39-50. <https://doi.org/10.1016/j.jphotochem.2017.03.027>
  55. Wahid F, Duan Y-X, Hu X-H et al (2019) A facile construction of bacterial cellulose/ZnO nanocomposite films and their photocatalytic and antibacterial properties. *Int. J. Biol. Macromol.* 132:692-700. <https://doi.org/10.1016/j.ijbiomac.2019.03.240>

56. Wang R, Hao Q, Feng J et al (2019) Enhanced separation of photogenerated charge carriers and catalytic properties of ZnO-MnO<sub>2</sub> composites by microwave and photothermal effect. *J. Alloys Compd.* 786:418-27. <https://doi.org/10.1016/j.jallcom.2019.02.009>
57. Wang Y, Geng Q, Yang J et al (2020) Hybrid System of Flocculation–Photocatalysis for the Decolorization of Crystal Violet, Reactive Red X-3B, and Acid Orange II Dye. *ACS Omega* 5:31137-45. <https://doi.org/10.1021/acsomega.0c04285>
58. Xiao H, Zhang W, Wei Y et al (2018) Carbon/ZnO nanorods composites templated by TEMPO-oxidized cellulose and photocatalytic activity for dye degradation. *Cellulose* 25:1809-19. <https://doi.org/10.1007/s10570-018-1651-4>
59. Xiao H, Zhang W, Wei Y et al (2018) Fabrication of Fe/ZnO composite nanosheets by nanofibrillated cellulose as soft template and photocatalytic degradation for tetracycline. *J Inorg Organomet Polym Mater* 28:1299-304. <https://doi.org/10.1007/s10904-017-0712-8>
60. Yang C, Xu W, Nan Y et al (2020) Fabrication and characterization of a high performance polyimide ultrafiltration membrane for dye removal. *J. Colloid Interface Sci.* 562:589-97. <https://doi.org/10.1016/j.jcis.2019.11.075>
61. Yi S, Cui J, Li S et al (2014) Enhanced visible-light photocatalytic activity of Fe/ZnO for rhodamine B degradation and its photogenerated charge transfer properties. *Appl. Surf. Sci.* 319:230-36. <https://doi.org/10.1016/j.apsusc.2014.06.151>
62. Yu J, and Yu X (2008) Hydrothermal synthesis and photocatalytic activity of zinc oxide hollow spheres. *Environ. Sci. Technol.* 42:4902-07. <https://doi.org/10.1021/es800036n>
63. Zhang B, Yang D, Qiu X et al (2020) Fabricating ZnO/lignin-derived flower-like carbon composite with excellent photocatalytic activity and recyclability. *Carbon* 162:256-66. <https://doi.org/10.1016/j.carbon.2020.02.038>

## Figures



**Figure 1**

Schematic presentation of the NC isolation from BS by acid hydrolysis process

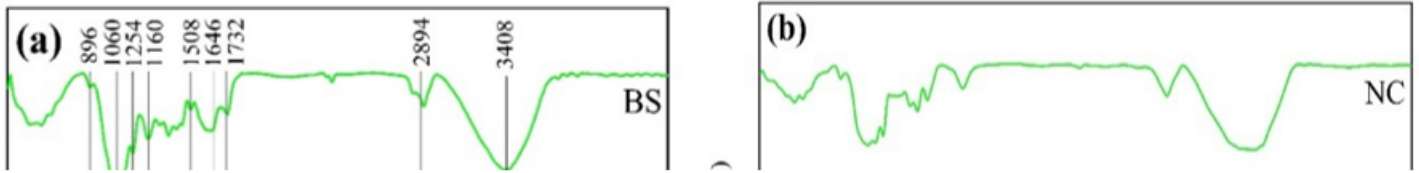


**Figure 2**

FTIR spectra of (a) BS, BBS, NC, (b) PZ, FZ1, and CFZ1-2

**Figure 3**

(a<sub>1</sub>–a<sub>3</sub>) FE-SEM images of BS, BBS and NC, respectively. (b<sub>1</sub>–b<sub>4</sub>) FE-SEM images of PZ, FZ1, FZ3, and FZ5, respectively. (c<sub>1</sub>–c<sub>4</sub>) FE-SEM images of CFZ1-1, CFZ1-2, CFZ1-3, and CFZ1-4, respectively, and (d<sub>1</sub>–d<sub>4</sub>) TEM images of NC, PZ, FZ1, and CFZ1-2, respectively

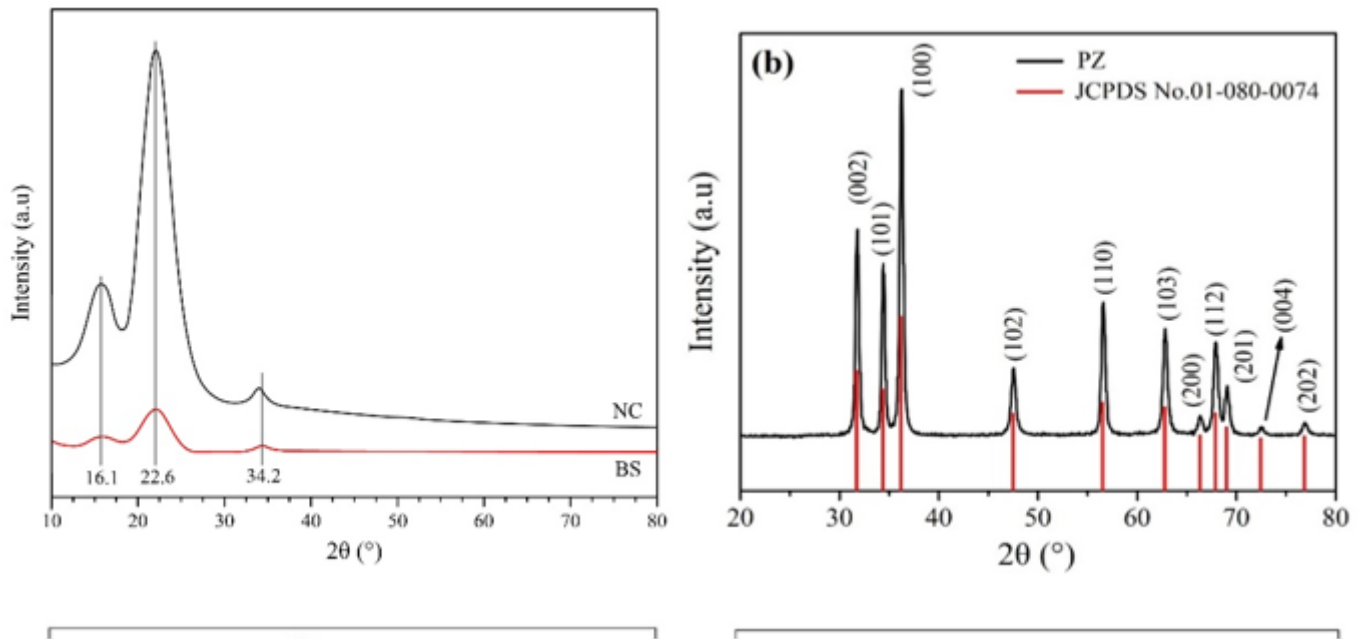


**Figure 4**

XRD patterns of (a) BS, and NC, (b) PZ, (c) FZs, and (d) CFZs

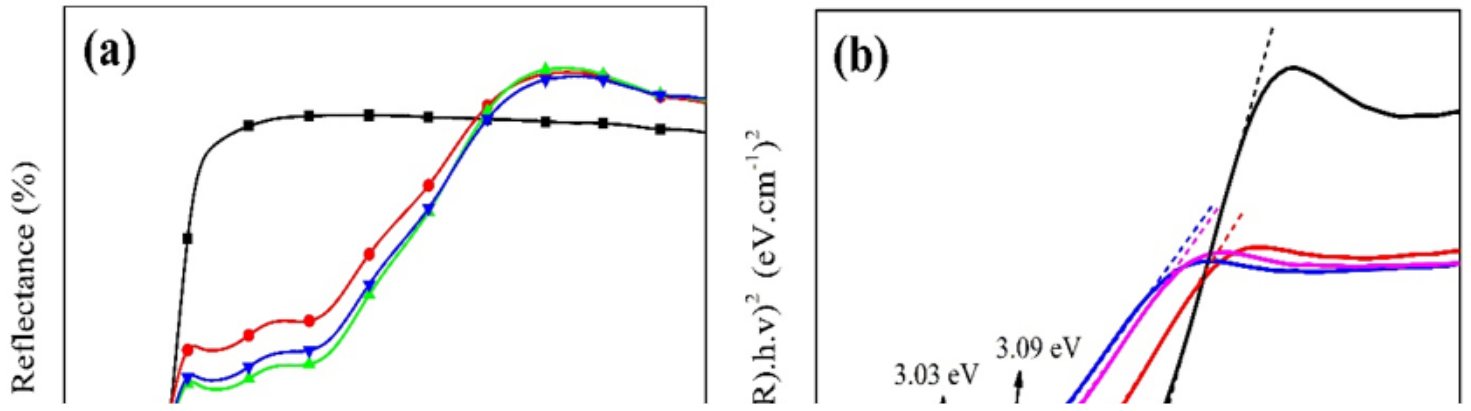


**Figure 5**

(a) Diffuse reflectance spectra, and (b) Kubelka-Munk transformed reflectance spectra of PZ, FZ1, FZ3, and FZ5



**Figure 6**

(a) TGA and (b) DTG profiles of NC, PZ, FZ1, and CFZ1-2

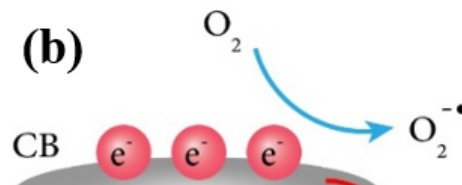


**Figure 7**

(a) Photocatalytic degradation of MB in aqueous solution using the PZ and FZs under UV light radiation and (b) schematic representation of photocatalytic mechanism of Fe-doped ZnO for MB degradation under UV light irradiation

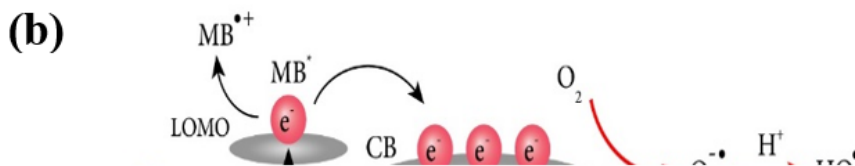
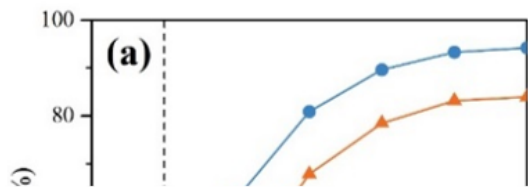


## Figure 8

(a) Photocatalytic degradation of MB in aqueous solution using the PZ and FZs nanoparticles under visible light radiation and (b) schematic representation of photodegradation mechanism of Fe-doped ZnO for MB under visible light irradiation

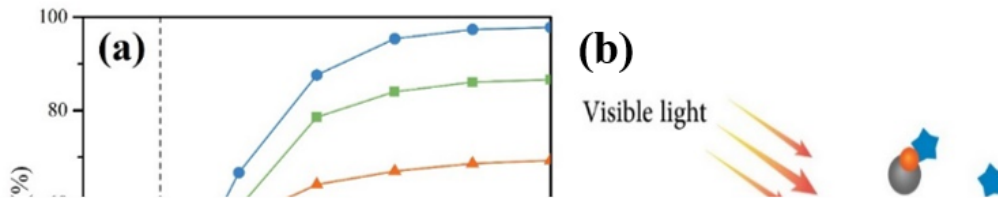


## Figure 9

(a) MB dye removal in the presence of CFZs and (b) possible hybrid mechanism of dye removal by the nanocomposites

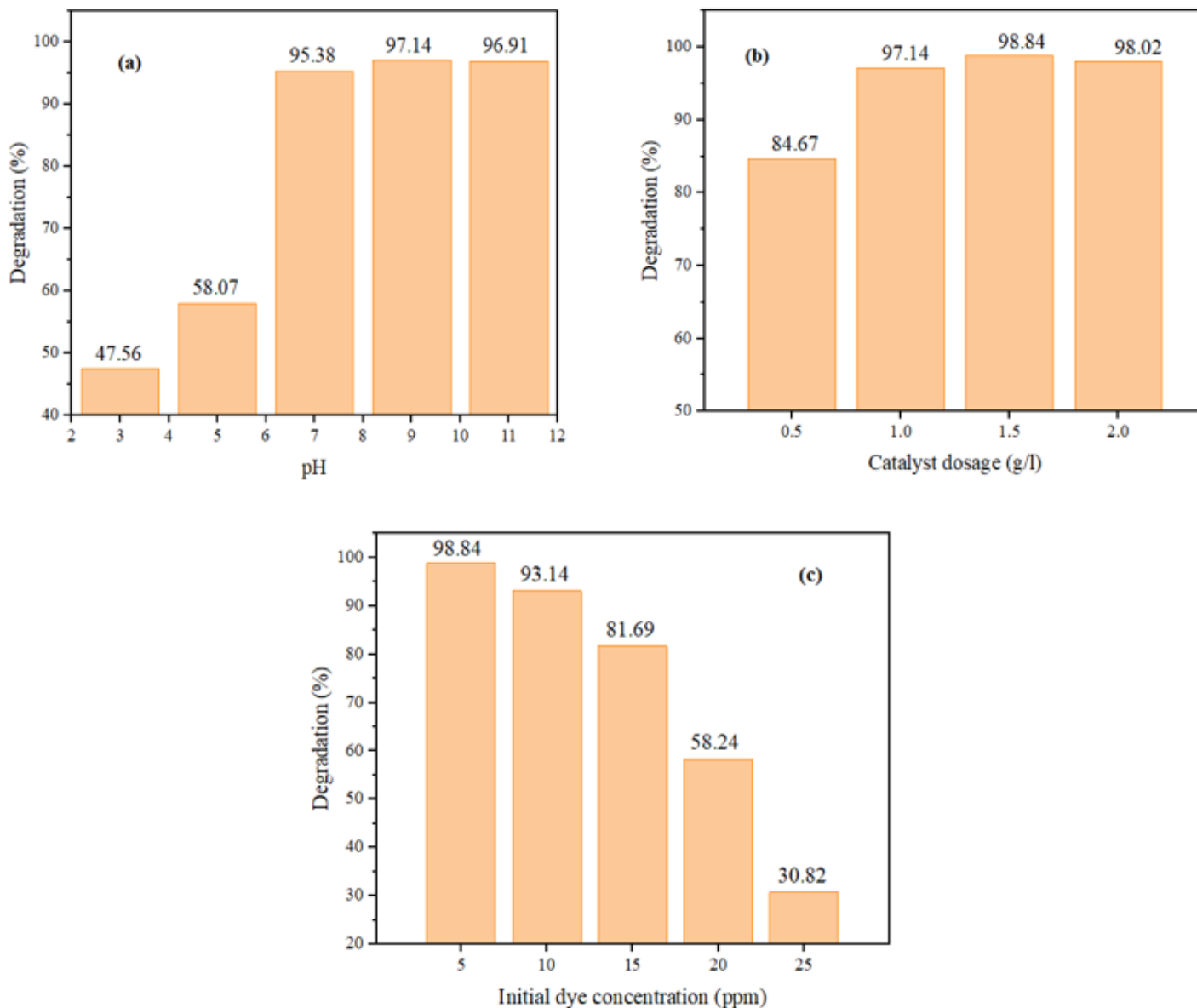


**Figure 10**

Effects of pH (a), catalyst dosage (b), and initial concentration of MB (c) on the MB degradation efficiency using CFZ1-2 (Fixed experimental parameters: 1 g/L of catalyst, pH of 9, and 5 ppm of MB at 90 min visible light irradiation)

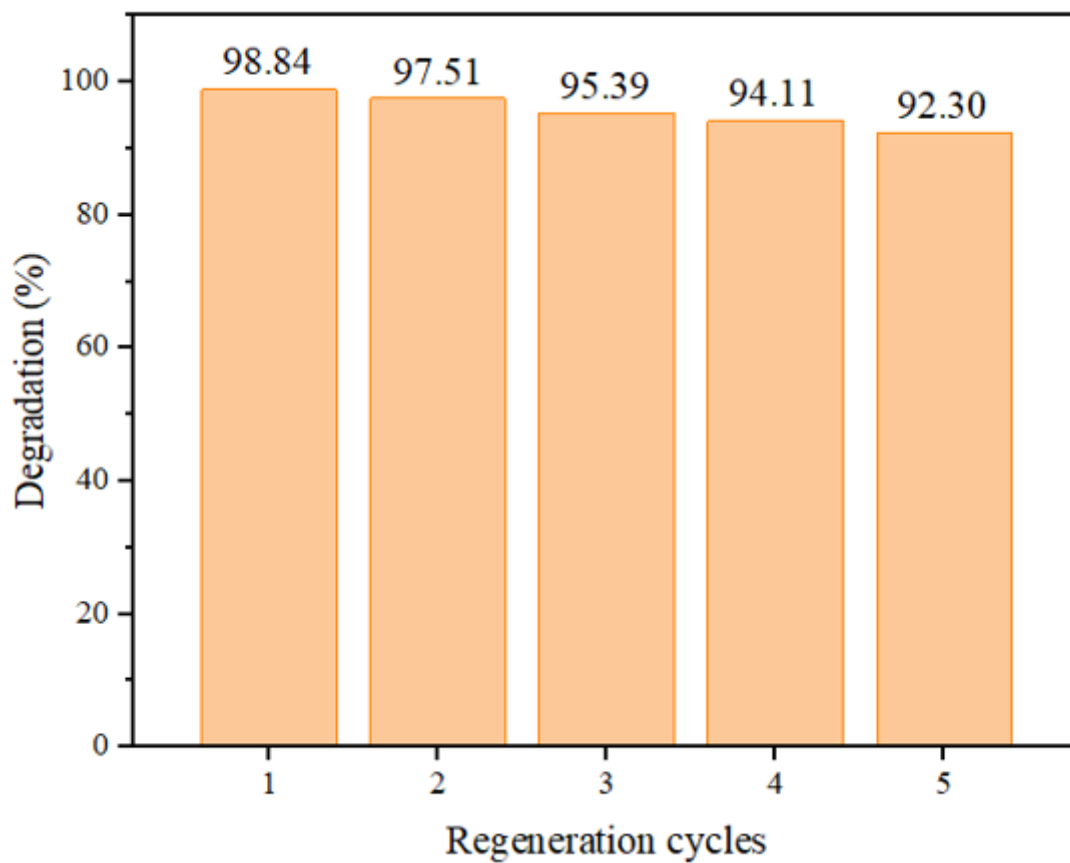


**Figure 11**

Recycling photocatalyst tests for CFZ1-2 nanocomposite under optimum conditions